

Low Temperature Opacities

Jason W. Ferguson¹, David R. Alexander¹, France Allard², Travis Barman¹, Julia G. Bodnarik^{1,3}, Peter H. Hauschildt⁴, Amanda Heffner-Wong¹, Akemi Tamanai^{1,5}

ABSTRACT

Previous computations of low temperature Rosseland and Planck mean opacities from Alexander & Ferguson (1994b) are updated and expanded. The new computations include a more complete equation of state with more grain species and updated optical constants. Grains are now explicitly included in thermal equilibrium in the equation of state calculation, which allows for a much wider range of grain compositions to be accurately included than was previously the case. The inclusion of high temperature condensates such as Al_2O_3 and CaTiO_3 significantly affects the total opacity over a narrow range of temperatures before the appearance of the first silicate grains.

The new opacity tables are tabulated for temperatures ranging from 30000 K to 500 K with gas densities from 10^{-4} g cm⁻³ to 10^{-19} g cm⁻³. Comparisons with previous Rosseland mean opacity calculations are discussed. At high temperatures, the agreement with OPAL and Opacity Project is quite good. Comparisons at lower temperatures are more divergent as a result of differences in molecular and grain physics included in different calculations. The computation of Planck mean opacities performed with the opacity sampling method are shown to require a very large number of opacity sampling wavelength points; previously published results obtained with fewer wavelength points are shown to be significantly in error. Methods for requesting or obtaining the new tables are provided.

Subject headings: atomic data — equation of state — methods: numerical — molecular data

¹Department of Physics, Wichita State University, Wichita, KS 67260-0032; jason.ferguson@wichita.edu; david.alexander@wichita.edu; travis.barman@wichita.edu

²CRAL-ENS, 46 Allée d'Italie, Lyon, 69364 France, Cedex 07; fallard@ens-lyon.fr

³Now at Gemini Observatory, 670 North A'ohoku Place, Hilo, HI 96720-2700; jbodnari@gemini.edu

⁴Hamburger Sternwarte, Gojenbergsweg 112, 21029 Hamburg, Germany; yeti@hs.uni-hamburg.de

⁵Now at Astrophysical Institute and University Observatory, Friedrich-Schiller-University Jena, Schiller-gaesschen 3, D-07745 Jena, Germany; akemi@astro.uni-jena.de

1. Introduction

When modeling the transfer of radiation through optically thick material, it is often useful to use pretabulated mean opacity tables, because performing computationally costly calculations of the frequency dependent opacity may not be feasible. There are many relevant applications in astrophysics for using mean opacities including the interiors of cool stars, giant planets, and disks of material forming stars and planets.

Recent opacity tables useful for modeling stellar interiors and envelopes come from two major sources, the OPAL opacities (Iglesias & Rogers (1991, 1993, 1996), Rogers & Iglesias (1992a, 1992b) and Rogers et al. (1996)) and the Opacity Project (Seaton et al. 1994, OP hereafter). The opacities from these two groups match very well at most temperatures, and their results have been used to resolve several discrepancies between theoretical models and observations including evolutionary models of high-mass stars (Stothers & Chin (1991)), interpretations of the HR diagram (Chiosi et al. (1992)) and radiative acceleration in stellar envelopes (Gonzalez et al. (1995)). Each of the above opacity databases are valid for temperatures greater than 6000 K, but do not include the effects of molecules which become important at lower temperatures.

In cool gases molecules become dominating sources of opacity and must be included in compilations of Rosseland opacity tables. Tsuji (1966) first included the effects of molecular absorbers such as H₂O, CO, and OH. The Wichita State University (WSU) low temperature opacity group began publishing tables of opacities for temperatures below 10000 K in 1975. Alexander (1975) computed opacities down to 700 K and included a crude estimate of the opacity due to dust grains. A better approximation to the dust opacity was included in Alexander et al. (1983) and Alexander & Ferguson (1994a, 1994b; AF94 hereafter). Sharp (1992) focused on molecular opacities and their application to accretion disks. Opacity tables for use in protoplanetary disk models were computed by (Semenov et al. 2003, S03 hereafter) for gas and dust mixtures from 10 K to 10000 K.

Table 1 illustrates the improvement in the WSU opacity calculations beginning in 1975 through the present. Current opacities are computed with a modified version of the stellar atmosphere code PHOENIX. Each of the changes indicated in the table will be discussed in one of the following sections starting with the equation of state followed by sources of opacity data. In Section 4 current opacities will be compared with AF94, OP, OPAL, and S03. Section 5 focuses on the computation of Planck mean opacity values. Methods of obtaining the new WSU opacity tables for the current set of compositions is described in Section 6 as well as how to request new or customized opacity tables.

2. Equation of State

As shown in Table 1 one of the most significant differences between the opacity tables of AF94 and current tables is within the equation of state (EOS hereafter). In AF94, only six grain species were included and their number densities were taken from pre-tabulated functions (percentage of grain material condensed) of temperature and pressure provided by Sharp (private communication). Consequently, AF94 used two decoupled equations of state, one for gas with grains and one for pure gas. While this procedure is reasonably accurate for compositions close to those provided to AF94 by Sharp (all of which have X (hydrogen) and Z (metal) abundances close to solar with differing C/O ratios), it becomes increasingly imprecise for compositions that deviate significantly from the solar mixture. Tests show that for nearly solar values of X the number abundances of grains in AF94 are consistent with the current work, however for a hydrogen poor gas differences do occur on the order of 20 times less grain material in AF94. The resulting mean opacity will subsequently be low by that factor, see below for a discussion of the mean opacity calculation.

The current EOS contained in the PHOENIX stellar atmosphere code most recently described in Allard et al. (2001) contains several hundred molecules and dozens of solid and liquid species in chemical equilibrium. The new EOS represents a significant advance in the calculation of low temperature molecular and grain opacities when compared to AF94. The EOS of PHOENIX is able to calculate the chemical equilibrium of 40 elements, including the ionization stages indicated in Table 2, along with the molecular and solid and liquid species for hundreds of species. For the discussion in this paper we focus on molecular and solid phase species, since liquids do not become abundant enough to affect the mean opacity.

Figure 1 shows the abundances of condensates as a function of temperature for a single gas pressure of 1 dyne cm^{-2} and a solar composition from Grevesse & Noels (1993). Several species have had their abundances summed for clarity. The silicate species MgSiO_3 , Mg_2SiO_4 , and Fe_2SiO_4 are combined with the minor species Na_2SiO_3 to make up the “Silicates” group. The “Fe” group contains both Fe- α and Fe- γ crystal structures. The four crystal structures of Al_2O_3 - $\alpha, \delta, \gamma, \kappa$ form the “ Al_2O_3 ” group. The “Titanates” group contains CaTiO_3 , MgTiO_3 and MgTi_2O_5 . The “Ca-Silicates” contains $\text{CaMgSi}_2\text{O}_6$, $\text{Ca}_2\text{Al}_2\text{SiO}_7$ and $\text{Ca}_2\text{MgSi}_2\text{O}_7$. The “Al-Silicates” group contains $\text{Al}_6\text{Si}_2\text{O}_{13}$, Al_2SiO_5 , KAlSi_3O_8 and $\text{NaAlSi}_3\text{O}_8$. The choice of each of the groups is arbitrary and is done only to make the figure more readable; such grouping is not done in the EOS or the opacity calculations of PHOENIX.

Figure 1 demonstrates the complicated nature of the equation of state for a cool gas. The first condensate to condense at the pressure shown in Fig. 1 is Al_2O_3 at about 1550 K (although ZrO_2 condenses at a higher temperature its abundance is not large enough to be shown in the figure). Below 1400 K Al_2O_3 disappears in favor of the “Ca-Silicates” group

(which does contain a small amount of Al) and the “Titanates”. Just at and below 1200 K “Silicates” and the “Fe” condensates form and dominate the abundance of grain material. The mean opacity of such a gas-grain mixture is discussed in Section 4.

The interplay between solid species and gas-phase chemistry is illustrated by focusing on abundant titanium species in Figure 2. Two separate calculations of the EOS are shown in the figure, one with grains and one without (“nog” in the figure). Both calculations assume solar abundances and a gas pressure of 1 dyne cm^{-2} . When condensation is included in the EOS the abundances of the molecular species are greatly reduced in favor of solid species. For example, molecular TiO, which is an important absorber in cool stellar atmospheres disappears when grains are included in the EOS. This removal will have a large impact on the opacity of the gas. The effect of removing an important species such as titanium via (for example) gravitational settling (see Allard et al. (2001) and Woitke & Helling (2004)) of solid particles can greatly affect the opacity.

Figure 3 shows a contour plot of the relative number abundance (the ratio of the amount of a particular species to the total gas density) of several species as functions of gas temperature and pressure. Fig. 1 represents a slice at $\log P = 0$ in Fig. 3. For clarity, each contour in Fig. 3 represents a single value of P_i/P_{gas} for each species, and has a different value for each species. The contour values shown are for Al_2O_3 (all four forms of Al_2O_3 are included) for which the value is -6.2; for CaTiO_3 the value is -7.0; for MgAl_2O_4 , -6.0; MgSiO_3 , -5.0; Fe, -4.7; and FeS is -5.0. The species with the highest condensation temperature at $\log P = 0$, Al_2O_3 , forms a ridge peaking along a line on $\log T = 3.0$ to 3.3 from low to high gas pressure. Note that at the very highest pressures the first condensate to form appears to be solid MgAl_2O_4 . However, because only a single contour value for each species is shown it appears as if Al_2O_3 does not exist at the highest pressures. This is artificial; Al_2O_3 still exists, but its abundance has fallen below the value of the contour shown. The species CaTiO_3 and MgAl_2O_4 also form ridges in the PT -plane, but very little MgAl_2O_4 forms at low pressures. Both MgSiO_3 and Fe condense on very broad plateaus: for example, Fe forms at temperatures lower than $\log T = 2.9$ at low pressures all the way up to $\log T = 3.35$ at the highest pressures. However, for the condensation sequence shown here the amount of solid Fe is reduced at $\log T = 2.7$ in favor of solid FeS.

A contour plot such as the one shown in Fig. 3 is important in understanding how the opacity changes with changes in gas temperature and pressure. As the gas-grain mixture turns from gas dominated to grain dominated the mean opacity changes dramatically: once grains “turn on” the mean opacity will also depend upon which grain exists and which do not. The following sections will discuss this relationship between the EOS and the opacity.

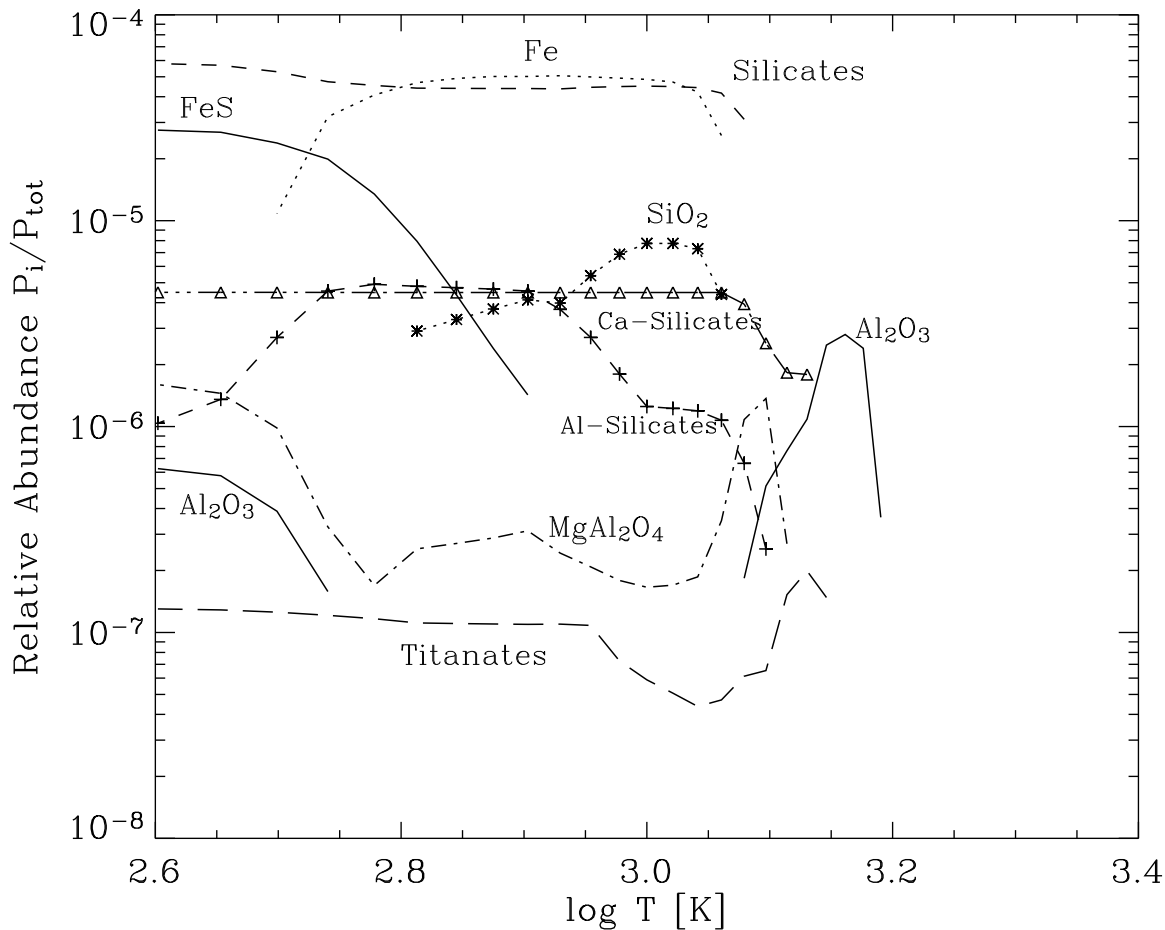


Fig. 1.— The relative abundances of different groups of grain species for a single gas pressure (1 dyne cm^{-2}) as a function of temperature. The choice of each group is arbitrary and is done only for clarity in this figure; the text describes the constituents of each group.

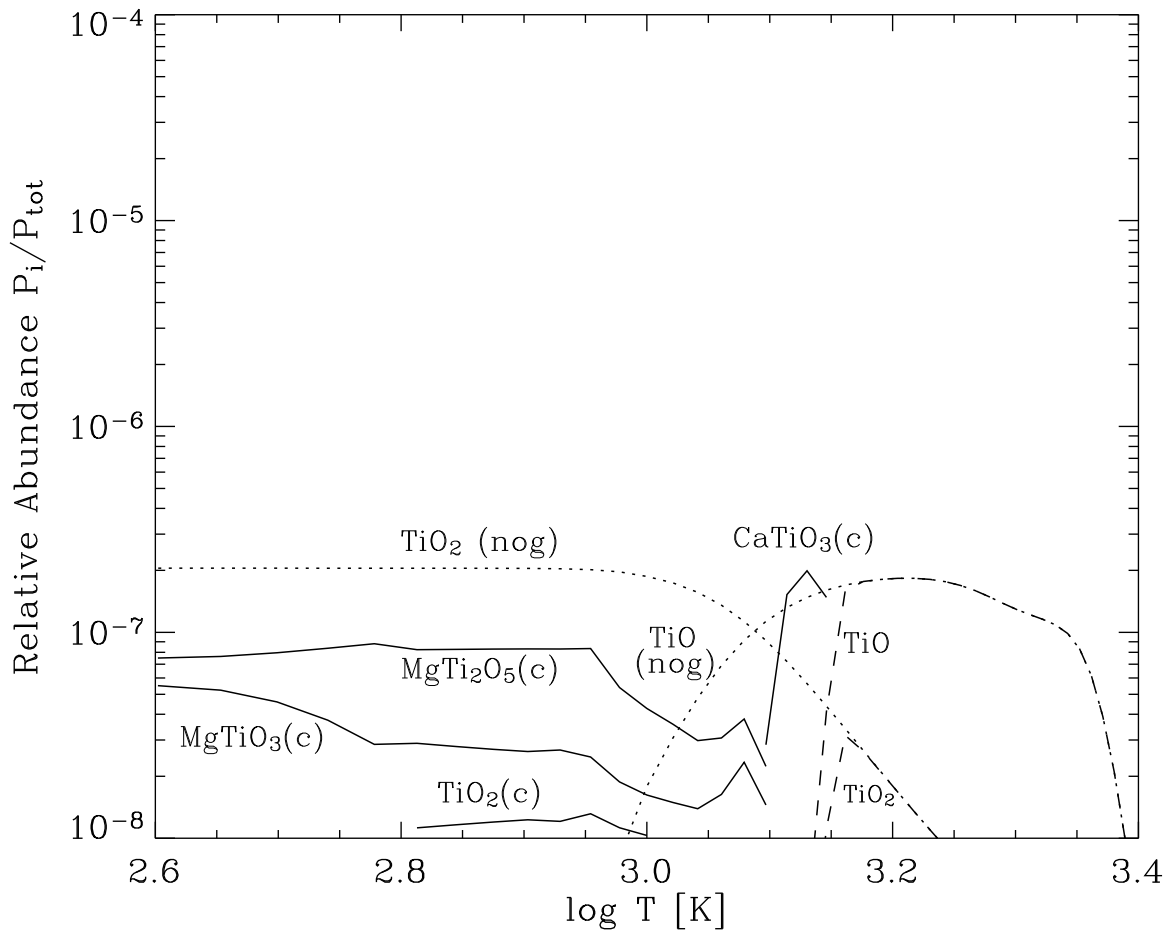


Fig. 2.— The relative abundances of Ti-bearing gas-phase and solid species for a single gas pressure (1 dyne cm^{-2}); the scale is the same as Fig. 1. The solid lines are the condensates and the long dashed lines are molecular TiO and TiO_2 . The dotted lines show the abundances of the molecular species when condensate species are *not* included in the calculation.

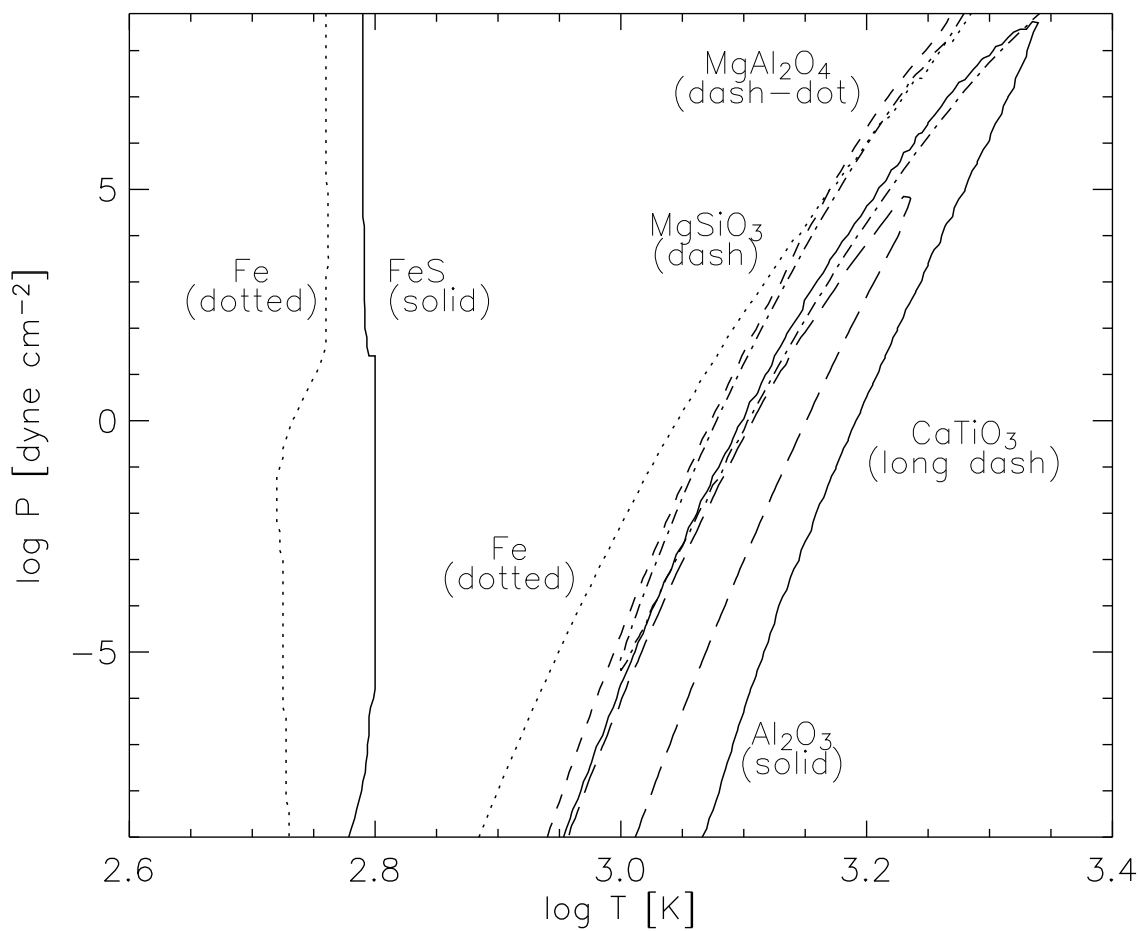


Fig. 3.— A contour plot of the abundance of several grain species as functions of gas temperature and pressure. The grains shown are Al_2O_3 (solid line, at high T), CaTiO_3 (long dashed line), MgAl_2O_4 (dash-dot line), MgSiO_3 (dashed line), Fe (dotted line), and FeS (solid line, at low T). As described in the text, only one contour value is shown for each species to make the plot more readable

3. Sources of Opacity

In the following sections we include a discussion of the sources of data for each type of opacity included in our calculations. Discussion of parameters in this section are based upon mean opacity tables computed for solar compositions with $3.3 \leq \log T \leq 4.3$ and from $-8 \leq \log R \leq 3$. The parameter R is defined as ρ/T_6^3 where ρ is the gas density and temperature is in millions of Kelvin.

The details of the calculation of the full table of Rosseland mean opacities is described in Section 4 below. Monochromatic opacities are used to compute the Rosseland mean (κ_R) by:

$$\frac{1}{\kappa_R} \equiv \frac{\int_0^\infty \frac{1}{\kappa_\lambda} \frac{\partial B_\lambda}{\partial T} d\lambda}{\int_0^\infty \frac{\partial B_\lambda}{\partial T} d\lambda} \quad (1)$$

where κ_λ is the monochromatic opacity described in this section, B_λ is the Planck function and $\partial B_\lambda/\partial T$ is therefore the weighting function of the Rosseland mean. For the computations discussed here we integrate Eq. 1 over 24,000 wavelengths. These wavelengths are not evenly spaced, and are concentrated between 0.1 and 2.0 μm : from 10 to 1000 Å we have points every 10 Å; from 1000 to 20000 Å, every 2 Å; from 20000 to 50000 Å, every 5 Å; from 5 μm to 50 μm , every 100 Å; and from 50 μm to 500 μm , points are spaced every 0.1 μm . The wavelength points are adjustable and several tests have been made to ensure convergence. For example, doubling the number of points increases the computation time by about a factor of two without significantly changing the total Rosseland mean opacity. Note that this is not the case for Planck mean opacities discussed in Section 5.

3.1. Continuous Sources

Descriptions of the continuous opacity sources used in PHOENIX are found in Allard & Hauschildt (1995). To be complete we list a few of the important sources here. For H, He and heavy elemental (C, N, O, Ca, Ti, V, Cr, Mn, Fe, Co and Ni) $b-f$ and $f-f$ atomic processes we use the cross-sections of Reilman & Manson (1979). For the other light elements we use the cross-sections of Mathisen (1984). The analytic fits of Verner & Yakovlev (1995) are also included in PHOENIX, but they are only significant at very high temperatures, beyond those discussed here.

The negative ions of a few elements can be large sources of $b-f$ and $f-f$ opacity. For H^- opacity we use John (1988) and for He^- we use a function from Vardya (1966)

which has been modified to reproduce the cross-sections from John (1994). For H_2^- we use a formula from John (1975). H_2^+ among other quasi-molecular hydrogen opacity sources are from Carbon & Gingerich (1969) and Gingerich et al. (1971). C^- opacities are from Myerscough & McDowell (1966).

3.2. Atomic Line Opacity

Table 2 shows the major atomic neutral and ionic species with strong spectral lines included in the work presented here. We include 40 atomic species and their ions in our calculations. Minor species such as Li, Be, and B among others are included in the EOS, but are not shown in the table since their low abundance and low number of lines do not affect mean opacities significantly. Since we focus on mean opacities calculated for temperatures less than 30000 K we do not include in our calculations ions beyond the 5th ionized stage for any element, but PHOENIX does have the capability to compute the opacity due to ions with higher ionized stages. Most of the line data is taken from Kurucz (1993), with small adjustments for minor species.

Often in model calculations it is convenient to discard weak lines to save computation time. The line selection process of PHOENIX is described in Allard & Hauschildt (1995), but for opacity tables computed by our group we include all atomic lines listed in Table 2 (plus weaker lines not shown in the table) with lines at line center having a line opacity larger than the opacity in the continuum as Voigt profiles. For lines weaker than the continuum we assume Doppler profiles. Schweitzer et al. (1996) contains a discussion of the details of this calculation.

3.3. Molecular Sources

Sources for the list of molecular lines used in PHOENIX are described in Table 3 for many individual molecular sources and in Table 4 for molecular line data from the HITRAN database from Rothman et al. (1992) and Husson et al. (1992). As in the computation of the opacity due to atomic lines, all molecular lines listed are read into PHOENIX; that is no line selection process is used. All molecular lines are assumed to have Doppler profiles since the number of molecular lines per wavelength interval is very large and no molecular lines are strong enough to have significant wings. As for the atomic lines Allard & Hauschildt (1995) and Schweitzer et al. (1996) contain discussions of the details of the calculation.

Water vapor opacity is a very strong source of opacity from about 1800 K to 2500 K. As

outlined in Table 3 PHOENIX has the ability to include three different water opacity sources. The earlier work of AF94 used the molecular line data from Jørgensen & Jensen (1993) and Jørgensen et al. (1994) for molecular water but this data is not available in our current code. For the opacities computed for this paper we have chosen to use the molecular line data from Partridge & Schwenke (1997) commonly used by various authors including Allard et al. (2001). This list has been shown by Allard et al. (2000) to provide a more complete description of the near-infrared spectra of brown dwarfs.

Collision-induced absorption (CIA) opacities are taken from data provided by the Borysow group. A detailed list of the references for the CIA opacities can be found in Allard et al. (2001) and Borysow (2002).

3.4. Grain Opacity

Just as is the case for molecules, the computation of the opacity due to small solid dust particles requires a knowledge of the abundance of the particles as a function of temperature and pressure and the absorption and scattering properties of each particle. The opacity due to a dust species can be computed from

$$\kappa_\lambda \rho = \pi \sum_i \int_a n_i(a) Q_{\text{ext}}(a, i, \lambda) a^2 da \quad (2)$$

where $n_i(a)$ is the normalized number of dust particles of species i of size a and $Q_{\text{ext}}(a, i, \lambda)$ is the total extinction (absorption plus scattering) efficiency of the particle. The size distribution, $n_i(a)$ depends upon both the number abundance of species i and the size distribution of dust particles. Here the size distribution of dust particles is assumed to be that found for particles in the interstellar medium by (Mathis et al. 1977, hereafter, MRN) also assumed by AF94. The choice of size distribution is somewhat model dependent and different distributions will change the resulting mean opacities. While an interstellar size distribution does not necessarily apply in other physical circumstances, it has been adopted as a standard by most investigators. Tables based upon other size distributions will be computed upon request. For a good review of modern size distributions, see Clayton et al. (2003). The extinction efficiencies of the particles is computed according to Mie theory for solid spheres composed of a single, pure substance. Future work will also explore the effect of different size distributions, aggregate grains, shape, and porosity on the mean opacity of gas-grain mixtures.

Table 5 lists the grain species included in our EOS and for which we have optical data

available. An excellent reference to an online database is found in Jäger et al. (2003b). The table gives each condensate by chemical formula, the source of the thermodynamic data, source of the optical constants and the wavelength range for which the optical data is valid. The last column in the table indicates if the data for the condensate is from an analog species. For example, optical constant data for MgTiO_3 is not available, but MgTiO_3 exists in the EOS and has a significant abundance for a narrow range of temperatures (see Fig. 2). Optical data for CaTiO_3 is available and can be used as an analog species for MgTiO_3 . The uncertainty in whether CaTiO_3 is a good analog for MgTiO_3 is much smaller than the error in including MgTiO_3 in the EOS with no opacity from that species.

For the computation of the Rosseland mean opacity, missing optical constant data over specific wavelength ranges will dramatically affect the resulting mean opacity due to the inverse nature of the Rosseland mean (see Fig. 16 of AF94). Often optical data is not available over the entire wavelength range that we integrate to compute the Rosseland mean. To avoid these problems we interpolate or extrapolate data so that the optical constant data covers the wavelength range from $0.1\mu\text{m} \leq \lambda \leq 500\mu\text{m}$. Care is taken in the extrapolation to follow trends in similar condensate species. For example, optical data for $\text{Ca}_2\text{Al}_2\text{SiO}_7$ is extrapolated into the visual part of the spectrum by using MgSiO_3 and Mg_2SiO_4 for comparison since all three species are silicate in nature and the far-infrared optical constants are similar in shape. While such extrapolations undoubtedly introduce uncertainties, however, the fact that the Rosseland mean weighting function is so small at short wavelengths (see Fig. 4f) these uncertainties are minor. We stress that $\text{Ca}_2\text{Al}_2\text{SiO}_7$ can be an important condensate at intermediate temperatures (see Fig. 1) and should not be removed from the mean opacity calculation.

4. Discussion of Results

4.1. Monochromatic Opacity

Monochromatic opacities of important absorbers are shown in Figure 4 for a range of gas temperature, a constant value of $\log R = -3$ and solar abundances. The important opacity contributors are indicated in each plot. The monochromatic opacities in each panel of the figure have been smoothed by convolving the monochromatic output of PHOENIX with a gaussian. The width of the gaussian varies with wavelength in order to show detail at a wide range of wavelengths. The wavelength range chosen is based upon the value of the weighting function (dB/dT); each plot is shown where the weighting function has a value greater than 0.1% of the maximum. As the temperature of the gas is decreased the wavelength maxima of the weighting function moves towards longer wavelengths as defined by $\lambda_{max} = 3600/T$.

It should be noted that the smoothing was only done in preparing these figures and is not done in the computation of the mean opacity.

In Figure 4a, at 10000 K, the frequency dependent opacity is dominated by hydrogen $b-f$ and $f-f$ absorption with a significant contribution from atomic line absorbers (labeled “metals” in the figure) appearing at short wavelength (typically $\lambda < 4000 \text{ \AA}$). The atomic line sources become even more important at shorter wavelengths, but the value of the weighting function is rapidly decreasing.

At 5000 K (panel b) the contribution of atomic lines increases significantly relative to the total opacity, while the opacity due to neutral hydrogen is diminished. At wavelengths longer than $0.5 \mu\text{m}$ H^- is the dominant continuous opacity source, but is not shown in panel (a) because it is not important at 10000 K. The contribution from molecular sources of opacity are not shown in panel (b) for clarity, but are included in the total opacity. The bump in the total opacity at $4.5 \mu\text{m}$ is due to CO gas, a molecule with high chemical stability.

In panel (c) of Fig. 4 at 2000 K the monochromatic opacity is beginning to be dominated by molecular absorbers. In the panel, the individual contributions from TiO, H_2O , and CO are shown. Between 4000 \AA and $1.2 \mu\text{m}$, TiO is the most significant contributor with CO being important at $4.5 \mu\text{m}$. Water opacity is the dominant source of opacity over the broad range of wavelengths shown in the panel. At 2000 K atomic metals are important below 4000 \AA , but are not important to the total mean opacity due to the sharp decrease in the weighting function.

At lower temperatures grains begin to become the dominant opacity source. Fig. 4d was chosen with a gas temperature of 1450 K (logarithm value 3.16) correlating to the peak of the Al_2O_3 abundance shown in Fig. 1. Fig. 4d shows how important a contribution Al_2O_3 can make. At many wavelengths Al_2O_3 is the strongest continuous contributor to the opacity with molecular sources adding a “forest” of lines on top of the dust source. Molecular sources still have a large role in the total opacity with TiO peaking at wavelengths shortward of $1.2 \mu\text{m}$ and H_2O contributing at infrared wavelengths.

At 1000 K the the most abundant grains are the silicates and iron (see Fig. 1). Fig. 4e shows how important grain sources of opacity can be to the total. Fig. 4f, with a gas temperature of 500 K, is shown indicating the strength of the individual contributors: solid Fe, FeS, and Silicate grains (for this figure the species MgSiO_3 , Mg_2SiO_4 , and Fe_2SiO_4 are included as “Silicates”).

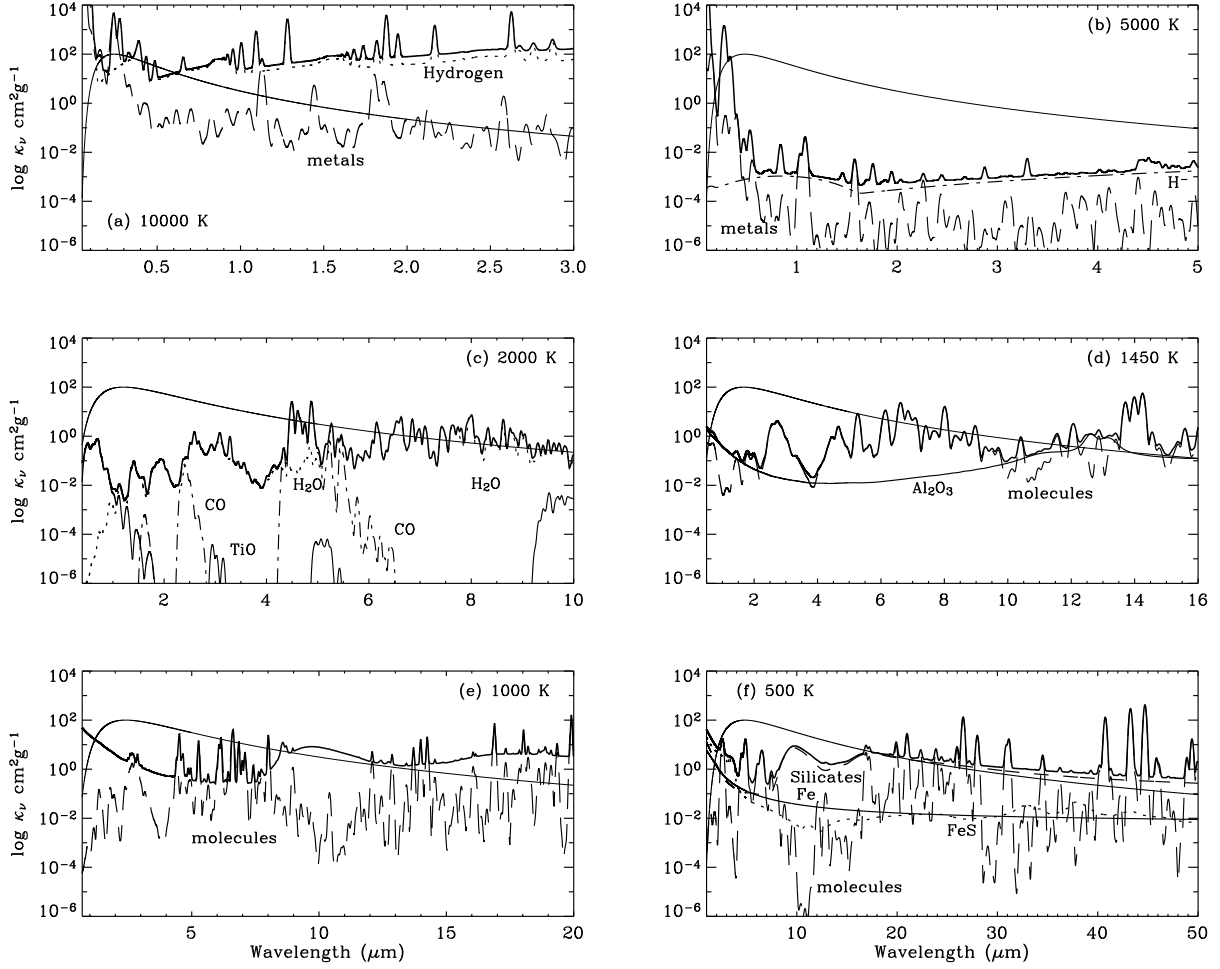


Fig. 4.— The monochromatic opacity at a wide range of temperatures for solar abundances and $\log R = -3$. Each panel is marked with the representative temperature and includes the weighting function, dB/dT (dotted line) used in the computation of the mean opacity. The wavelength range of each plot is shifted so that the weighting function is within 0.1% of the maximum and the monochromatic opacities were smoothed by convolving the monochromatic output of PHOENIX with a gaussian. See text for a detailed discussion of each panel.

4.2. Pure Hydrogen Case

Shown in Figure 5 is the mean opacity from this work compared with OPAL and AF94 for the pure hydrogen case for $\log R = -3, -1, \text{ and } 1$; pure hydrogen opacities are not available from OP. Results are generally quite good, with differences between OPAL and this work being 0.02 dex for the temperatures shown in the plots for low $\log R$ values. For the larger $\log R$ values the difference is as large as 0.05 dex or 12%. When we remove opacity sources from our calculations including all molecular hydrogen species (H_2 , H_2^- , etc.) and quasi-molecular hydrogen opacity, then mean opacities at the higher $\log R$ values compare much better with OPAL. The rise in our opacity at lower temperatures (about 5600 K) is due to our inclusion of molecular hydrogen which is not included in OPAL.

4.3. Pure Helium Case

A comparison between OPAL, OP, and AF94 with present calculations for the pure helium case are shown in Figure 6a. Again the values of $\log R$ are indicated in each panel. A large difference is apparent between $3.9 < \log T < 4.4$ where the mean opacity from this paper is much higher than either AF94 and OPAL. The cause of this effect is our inclusion of neutral helium absorption lines which are not included by OPAL, OP, or AF94. Fig. 6b shows this effect with the same ratios as Fig. 6a, but without neutral He lines included in the computation. Notice that the scale of the figure is different than in Fig. 5. At mid-range temperatures the opacity differences are similar in absolute magnitude to the pure hydrogen case.

4.4. Zero-metallicity Case

Figure 7 presents the results for a hydrogen and helium mixture, specifically $X = 0.7$ and $Z = 0$. As in the pure hydrogen and the pure helium mixtures the comparisons are good. Differences between our opacities and those from OPAL are within 0.03 dex from $3.9 < \log T < 4.3$ for low $\log R$ values. Comparing with OP, differences are as large as 0.07 dex in the same temperature range. This indicates conflicting results between OPAL and OP (see the recent paper by Seaton & Badnell 2004). Differences increase at lower temperatures as molecular hydrogen becomes important in our opacity calculations (see the discussion above for a pure hydrogen case).

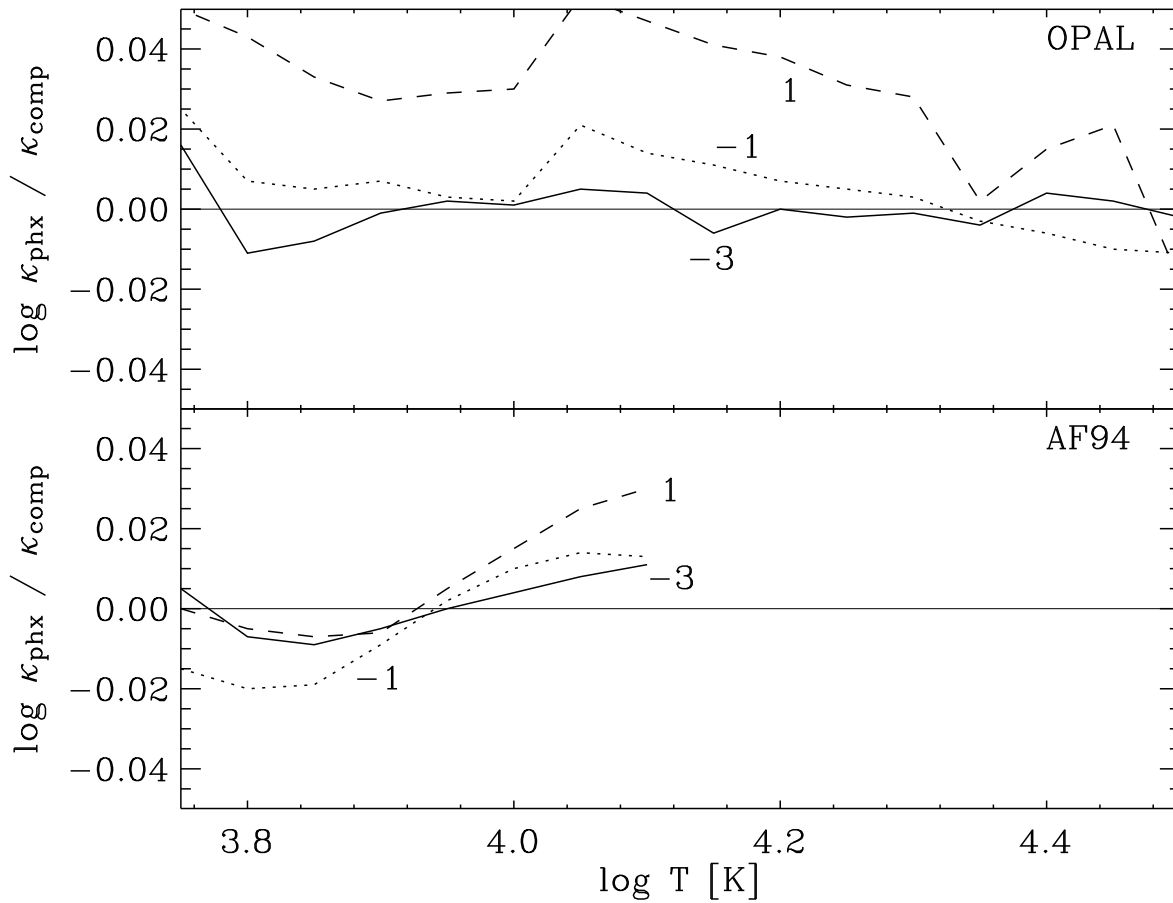


Fig. 5.— Plot of the logarithm of the mean opacity ratio for various values of $\log R$. For clarity each ratio is marked with its value of $\log R = -3$ indicated as solid lines, -1 as dotted lines and $\log R = 1$ as dashed lines. AF94 opacities are not available for $\log T$ values larger than 4.1.

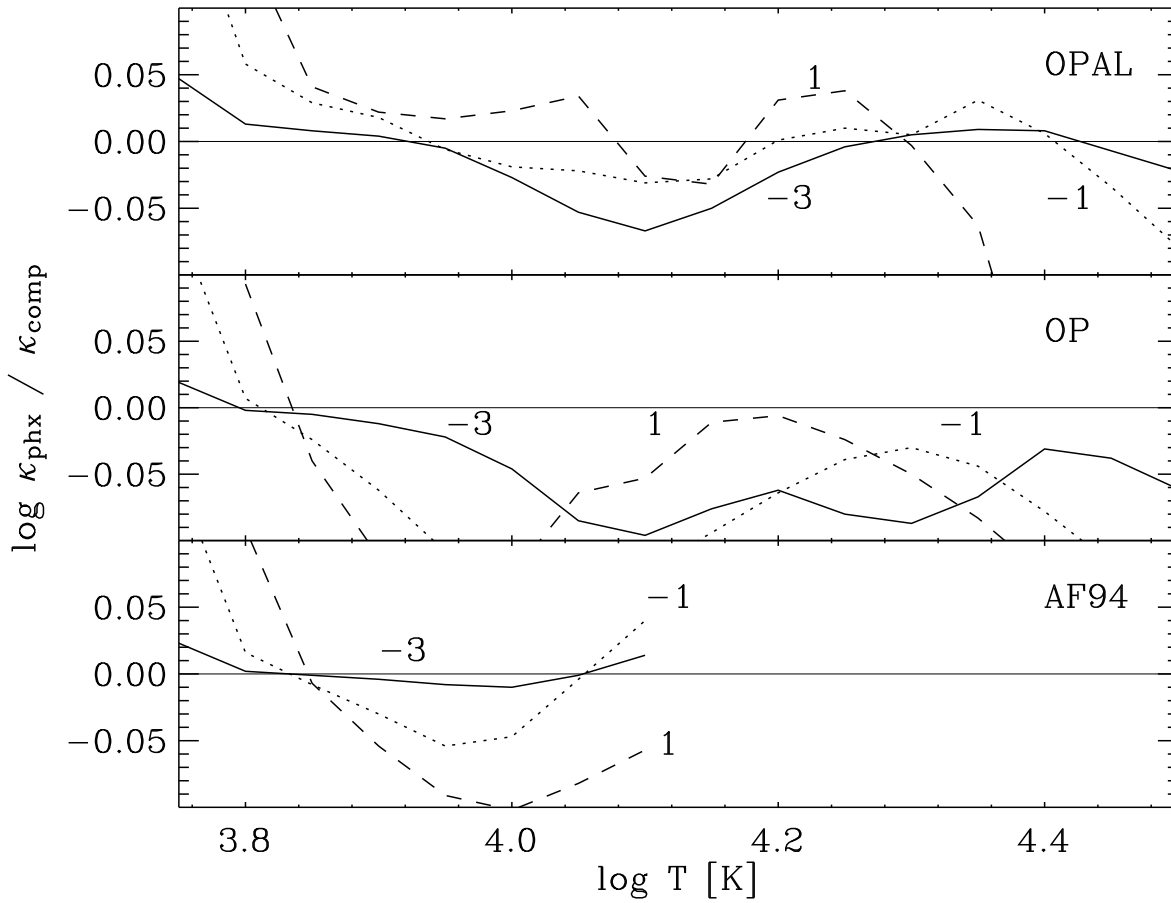


Fig. 6.— The upper panel is the same as Fig. 5 (with the exception of the vertical scale) for the pure He case. Large deviations in the opacity ratio are discussed in the text. The lower panel is the same as the upper panel except the opacity due to He lines is not included in the computations.

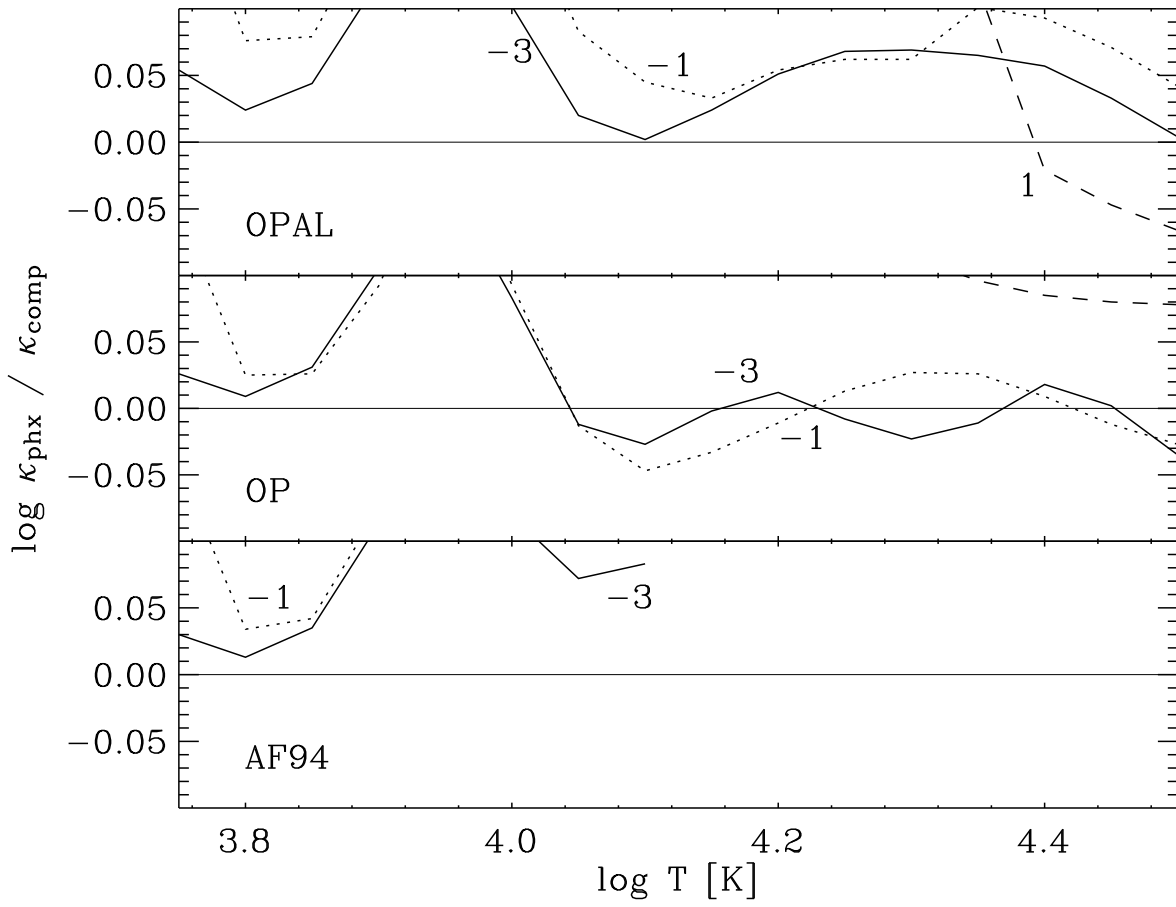


Fig. 6.— Fig. 6b

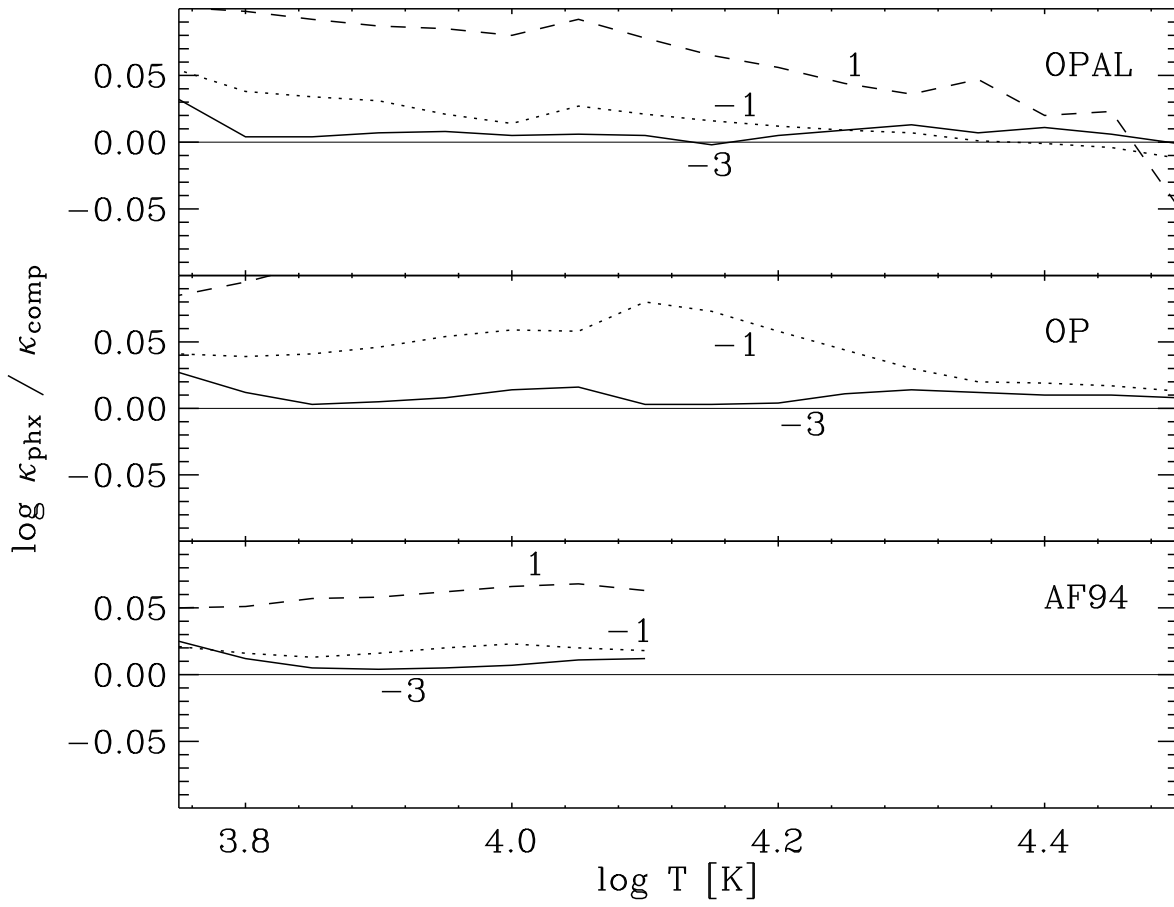


Fig. 7.— Same as Figure 5 for the zero-metallicity case

4.5. Solar Metallicity Case

Shown in Figure 8 are comparisons for the solar metallicity case $X = 0.7$ and $Z = 0.02$ for the same $\log R$ values used in previous figures. Again, differences are generally less than 0.05 in the logarithm of the mean opacity for $\log T$ values larger than 4.1. At lower temperatures the effects of molecules on the equation of state begin to become important.

Figure 9 shows the Rosseland mean opacity for solar abundances ($X=0.7$, $Z=0.02$ based upon Grevesse & Noels (1993)), temperatures from 500 K to 10000 K, and for $\log R = -3.0$. Opacities from OP, OPAL and S03 are also shown in the plot. The features seen in the figure come from the physics discussed in Figures 1 (the EOS) and 4 (monochromatic opacity) and the regions where grains, molecules, and atoms dominate the opacity are also indicated in the figure. At high temperatures atomic line and continuous opacities dominate the Rosseland mean which falls towards cooler gas temperatures as the atoms become more neutral. A bump is seen at $\log T \sim 3.6$ where molecules begin to become important. The sharp rise seen to the left of $\log T \sim 3.4$ is due to the formation of molecular H_2O and TiO (see Fig. 4c). The bump peaks at $\log T \sim 3.3$ and begins to fall again due to decreased population of excited levels in molecules. Grains appear at $\log T \sim 3.16$ (at this gas pressure) as shown in Fig. 1. For different gas pressures the appearance temperature of grains will move cooler at low pressure and move warmer at higher pressures as shown in Fig. 3. The appearance or disappearance of various grain species account for the rise and fall of the mean opacity towards cooler temperatures in Fig. 9. Many of the individual features will be discussed in detail below.

Several differences between the sets of opacities are readily apparent, the largest being at low temperature with some minor differences in the region dominated by atomic opacities. At higher temperatures AF94, OP, OPAL and the current work are not resolved in the figure, however, mean opacities from S03 are seen to be somewhat lower than the others. Fig. 8 shows that differences between AF94, OP and OPAL are all less than 0.05 in the logarithm. The difference between the current work and S03 is 0.17 dex at $\log T = 3.8$, or nearly 50% lower in value. Second, the effect of the absence of molecules in the OP calculation becomes apparent around $\log T \sim 3.6$. The dominant opacity source from $\log T = 3.25$ to 3.4 is line opacity from molecular water and TiO . Third, the onset of grain formation, seen at $\log T = 3.25$ in Fig. 9, occurs at a lower temperature in AF94, and even lower in S03. This difference is the result of the more complete gas/grain EOS included in the present work while, as already mentioned, AF94 only included six grain species in the EOS. Also both AF94 and S03 do not include high temperature condensates such as Al_2O_3 . In trial computations where the higher temperature condensates were not included, the trend shown by S03 was well matched. Another small factor in the differences between this work and S03

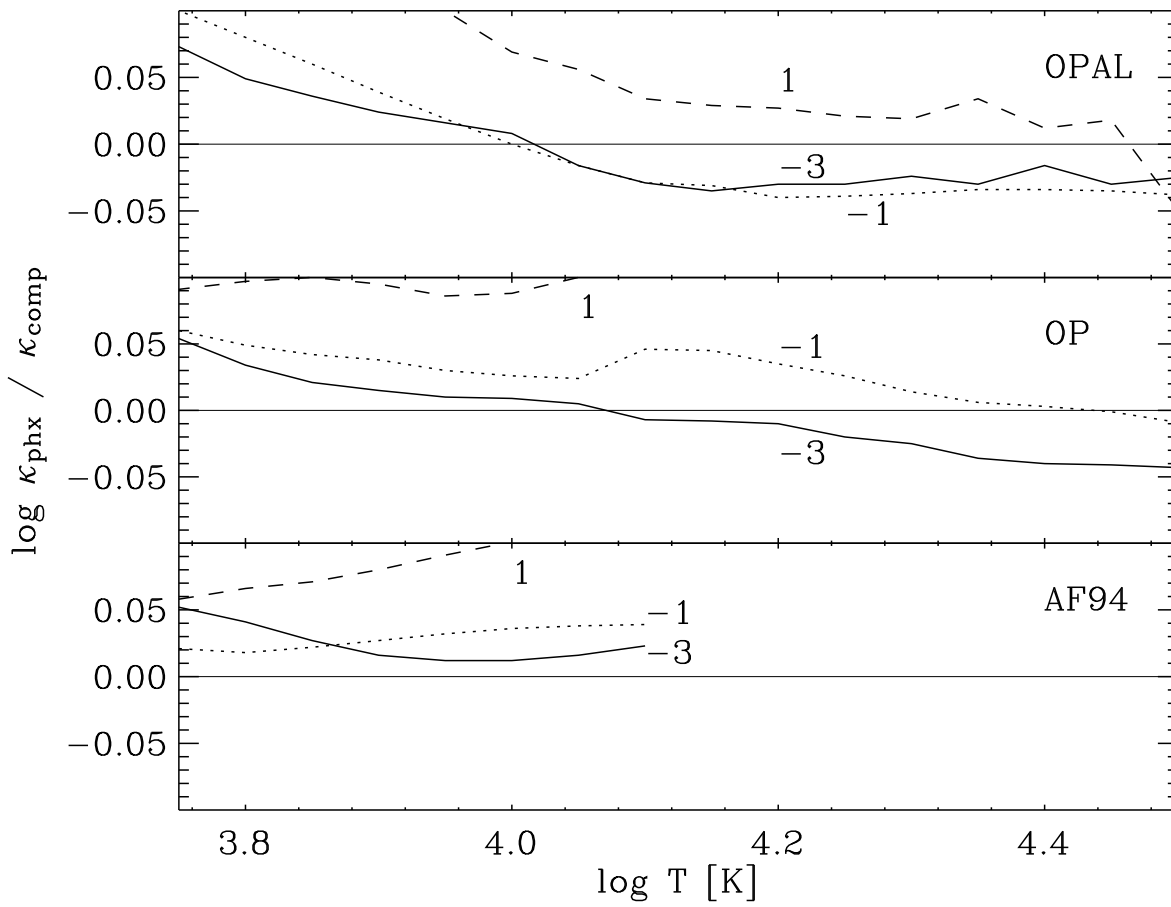


Fig. 8.— Same as Figure 5 for solar metallicity abundances.

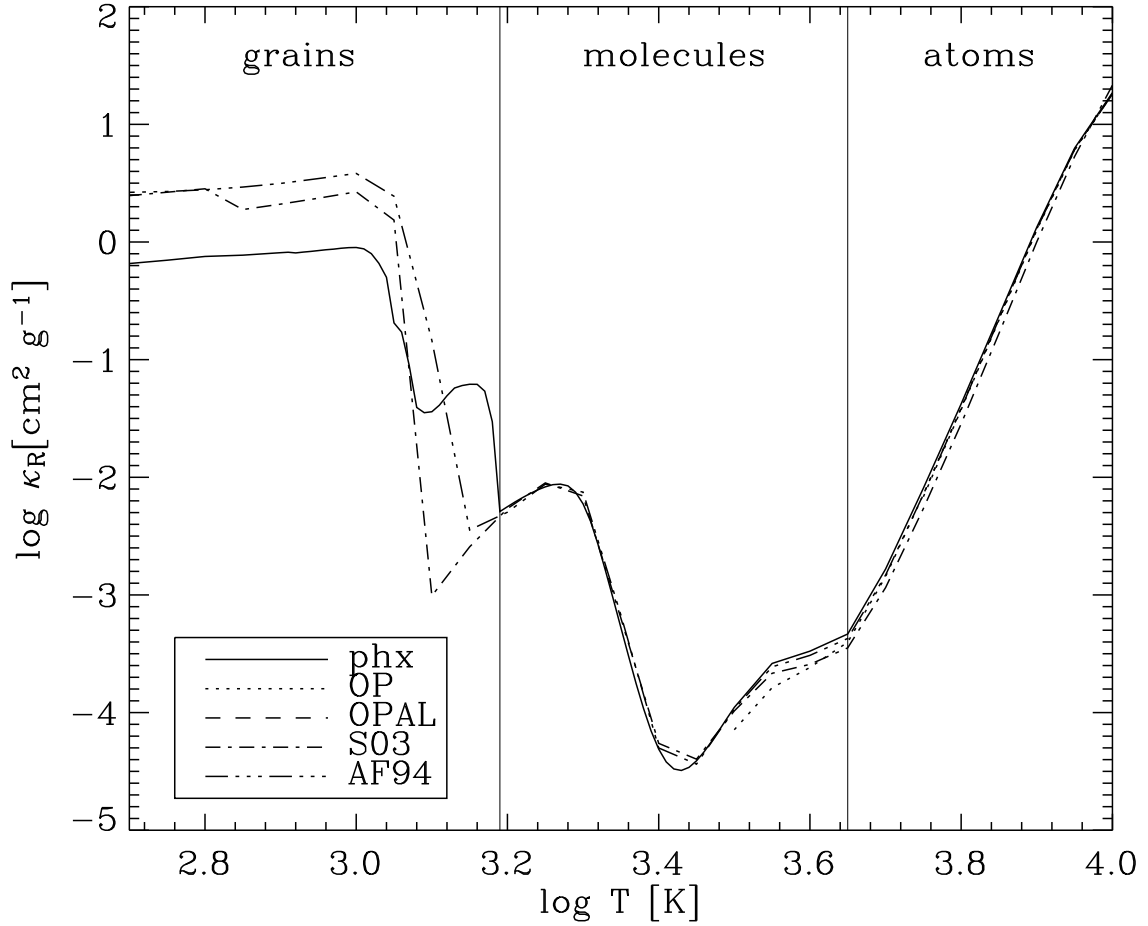


Fig. 9.— Logarithm of the Rosselland mean opacity as a function of temperature for various computation of the opacity as indicated in the legend. The computation is for solar abundances and $\log R = -3$. Regions where certain species grains, molecules, and atoms dominate the opacity are indicated. Differences at low temperature are discussed in the text.

is the use of condensation temperature instead of evaporation temperature. In a physical circumstance where the temperature is time-dependent, these two temperatures do not have the same value due to a hysteresis-like effect: the evaporation of grain material occurs at a temperature lower than the condensation temperature, as discussed by S03.

A difference of greater concern in Fig. 9 is the magnitude of the Rosseland mean opacity at low temperatures when comparing with AF94. At $\log T = 3.0$ AF94 has a Rosseland mean opacity that is about half a dex greater than present calculations. There are several reasons for this large difference. First, the computations of AF94 utilized a crude EOS (only six grains species and decoupled grain and gas number densities) and do not match the number abundances of the current EOS. Second, AF94 used the continuous distribution of ellipsoids (CDE) for computation of the grain opacity which produces a greater total opacity from a fixed amount of grain material. Third, AF94 used optical constants from Ossenkopf et al. (1992) for (dirty) astronomical silicates while the current data set is outlined in Table 5. When we change the input optical constant data for silicates in PHOENIX to match that of AF94 we come much closer to repeating the results of AF94. Since the EOS of PHOENIX computes the amount of individual species of pure enstatite, forsterite, and fayalite we use the optical constants for those pure solids and try not to mix in "astronomical silicates" or use data for olivine ($(\text{Mg,Fe})_2\text{SiO}_4$).

Comparing present opacities with S03 presents challenges as well. The S03 paper includes a variety of models for dust parameters and for Fig. 9 we used the S03 model that best fit the assumptions of our current calculations, including that grains are homogenous spheres with a normal iron content. Other differences between this work and S03 are due to differences in the optical constant data used, different EOS methods, and different grain size distributions.

The importance of the various grain opacity contributors is demonstrated in Figure 10. In the figure the partial Rosseland mean opacity is shown: that is, the total opacity is computed excluding one species at a time is plotted. It is important to point out that in both panels of Fig. 10 the opacity source is removed, but each species still exists in the EOS. Removing the species from the EOS can introduce drastic changes to the abundances of other species and effect the mean opacity in non-linear ways.

In Fig. 10a there are only three dominant opacity sources shown. Hydrogen contributes the most at temperatures above 5000 K. For temperatures less than about 10000 K the continuous opacity due to the H^- molecule is very important, while below 5000 K molecular sources dominate the mean opacity.

Lower temperature partial opacities are shown in Fig. 10b. Again the solid line is the

mean opacity with all species, the dash-dot line removes all molecules from the opacity, the dashed line removes only water opacity and the dotted line (only for $\log T$ larger than 3.2) removes the contribution of molecular TiO. Notice that removing molecular sources changes the mean opacity by more than a factor of 1000 at $\log T = 3.3$. At even lower temperatures removing all grain species (see the dash-dot-dot-dot line in Fig. 10b) from the opacity has a dramatic effect on the mean opacity, for example at $\log T = 2.8$ the difference is more than six orders of magnitude. In Fig. 10b the dotted line (below $\log T = 3.1$) is the opacity without silicate grain sources, and the long dashed line is the opacity without condensed iron.

4.6. Metallicity Dependence

Figure 11 shows the effect on the opacity due to changes in metallicity. For $\log R = -3$ changes in the amount of metals as a function of Z are shown in Fig. 11a and changes with amount of hydrogen (X) are shown in Fig. 11b. For the variable Z case, notice that not only is the total opacity diminished as the amount of metals is reduced, but that condensation temperatures are also reduced since there are less metals available for grains to exist in equilibrium. For $Z=.1$ the onset of grains occurs at about $\log T = 3.2$, but for a highly reduced metallicity, $Z=.0001$, the onset occurs at about $\log T = 3.1$, more than 300 K cooler than the higher Z value. Even though the amount of metals has been reduced by three orders of the magnitude at these gas temperatures the amount of the Rosseland opacity has been reduced by more than four orders of magnitude. When grains exist they are a powerful opacity source.

In Fig. 11b with constant Z and variable X the grain formation temperatures are about the same since hydrogen is in such great abundance and does not play a role in the grain chemistry. The amount of opacity seen at the higher temperatures is greatly affected however, as the hydrogen fraction is reduced and the abundance of helium is raised especially at $X=.1$ and helium lines dominate the opacity at gas temperatures larger than 15000 K. The molecular bump seen at $\log T \sim 3.6$ (Fig. 9) is slightly reduced as is the rise due to molecular H_2O at $\log T \sim 3.4$ since there is less hydrogen available. The rises in the opacity due to condensates is slightly affected with the formation temperatures ($\log T \sim 3.2$) being slightly higher with less hydrogen to form water.

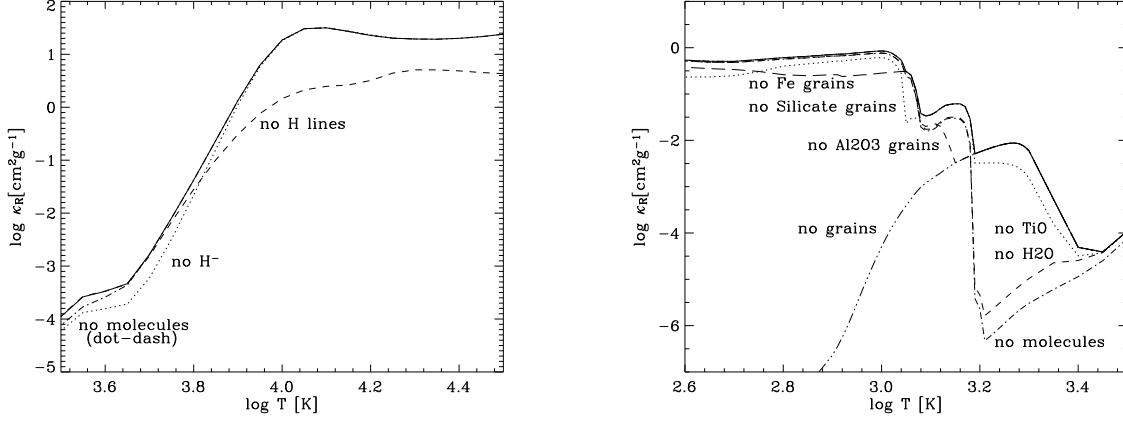


Fig. 10.— Partial Rosselland mean opacity for $\log R = -3$ with several opacity sources removed one at a time from the computation. In the upper figure the high temperature sources are shown. The solid line is the total opacity, the dashed is with H $b - f$ and $f - f$ sources removed, the dotted line removes H^- , and the dash-dot line contains no molecules in the computation. Similarly in the lower figure each of the lines are marked with the source that has been removed. See text for a complete discussion.

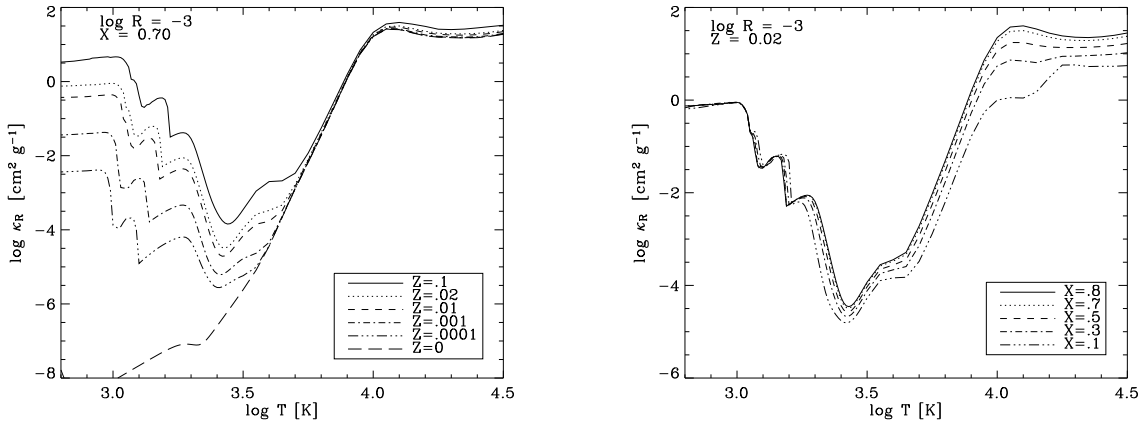


Fig. 11.— Rosselland mean opacity as a function of metallicity (panel a) and hydrogen fraction (panel b). In panel (a) lines refer to the total opacity with $X=0.7$, held fixed, and with the values of Z indicated in the legend. In panel (b) the lines refer to the total opacity with $Z=0.02$, held fixed, and with X indicated in the legend.

5. Planck Mean Opacities

The Rosseland mean opacity is often used in the limit where the diffusion approximation is a valid description of the physical conditions of a gas, typically in optically thick regions. In optically thin regions the diffusion approximation may not be a valid approximation. In such cases the Planck mean opacity (κ_P) can be used to represent the mean opacity and is defined as

$$\kappa_P \equiv \frac{\int_0^\infty \kappa_\lambda B_\lambda d\lambda}{\int_0^\infty B_\lambda d\lambda} \quad (3)$$

where variables are defined as in Eq. 1. The main difference between a Rosseland and Planck mean opacity is the way in which the monochromatic opacity is averaged. In the case of a Rosseland mean, the inverse of the opacity, multiplied by $\partial B/\partial T$, is summed making the total mean a harmonic mean, that is, the mean heavily weights wavelengths of low opacity, such as gaps between lines. For the Planck mean the monochromatic opacities, multiplied by the Planck function, are summed directly, so that the total mean Planck opacity is a representation of the opaqueness of the gas rather than its transparency.

Figure 12 shows a comparison between our calculations and a representation of calculations from the literature (including OP, S03, and Sharp (1992)). Note that the figure is for a single gas density of 10^{-10} g cm $^{-3}$ and not in log R space. Also included in Fig. 12 is a PHOENIX computation with more than one million wavelength points, more than 40 times the normal wavelength set as defined in Section 3. The normal wavelength set of 24,600 wavelengths is not sufficient to match the computation from OP. It is the opacity sampling method of atomic lines (and molecular lines at lower temperatures) employed in our calculation that causes this deficiency. This effect is fully expected due to the way in which OP computes the Planck mean opacity; they essentially sum the oscillator strengths for each line (Seaton, private communication) removing the uncertainty of line profile shape and wing cutoffs.

What is puzzling about Fig. 12 is the nearly five order of magnitude difference between the Planck opacities of OP and S03 at high temperatures where atomic line sources dominate the mean opacity. At low temperatures when the opacity of the gas is dominated by continuous dust sources the results are very similar. AF94 opacities are high due to the use of the CDE for the calculation of the grain opacity. We can account for differences at high temperature between our work, AF94 and OP because of our use of opacity sampling for line opacities and the number of wavelengths points used. It is speculated that S03 and Sharp (1992) are different from the current work due to differences in the molecular line lists used,

EOS and number of wavelengths over which the mean opacity is integrated.

The final point we wish to make is that users of AF94 Planck opacities need to strongly consider using our newer Planck opacities computed with over one million wavelength points. The newer calculations nicely overlap with OP at higher temperatures and we are confident of their validity as shown in Fig. 12.

6. New Opacity Tables

Many updates have been made to the previous WSU low temperature opacity tables. AF94 was only valid below 12000 K, while current tables are valid up to 30000 K and there is better agreement with OP and OPAL at high temperatures than AF94. The present work includes many more wavelength points in the calculation of the mean opacity and includes a greater number of molecular lines for most sources than AF94, most of which are based upon improved laboratory observations and quantum mechanical calculations. For dust species, the EOS of the dust is now fully coupled to the gas. Many more dust species are also included in the current work.

The standard set of opacity tables that we compute range from $2.7 \leq \log T \leq 4.5$ in 0.05 dex increments above $\log T > 3.5$ and below $\log T < 2.9$. Between those temperatures the stepsize is 0.01 dex in order to gain resolution of the discontinuities at the grain formation boundaries. For the density parameter R we compute tables with a range $-8 \leq \log R \leq 1$ in steps of 0.5 dex. Each table contains 75 temperature and 19 density points for a total of 1425 computations.

For chemical abundances, our base mix is based upon Grevesse & Noels (1993) and is then scaled to $X = 0.0, 0.1, 0.2, 0.35, 0.5, 0.7, 0.8, 0.9$ or $Z = 0.0, 0.00001, 0.00003, 0.0001, 0.0003, 0.001, 0.002, 0.004, 0.01, 0.02, 0.03, 0.04, 0.06, 0.08, 0.1$ for a total of 120 abundance tables in each set.

Opacity tables for the base set are available for download at our web site available at <http://webs.wichita.edu/physics/opacity>. Custom abundance sets are available upon request as are tables in density space rather than $\log R$ as well.

Low temperature astrophysics at Wichita State University is supported by NSF grant AST-0239590, NASA LTSA grant NAG5-3435, NASA EPSCoR grant NCC5-168 and NSF EPS-9874732 with matching support from the State of Kansas. We are most grateful to the referee, D. Semenov, for insightful comments on the manuscript. PHH was supported in part by the Pôle Scientifique de Modélisation Numérique at ENS-Lyon. Some of the calculations

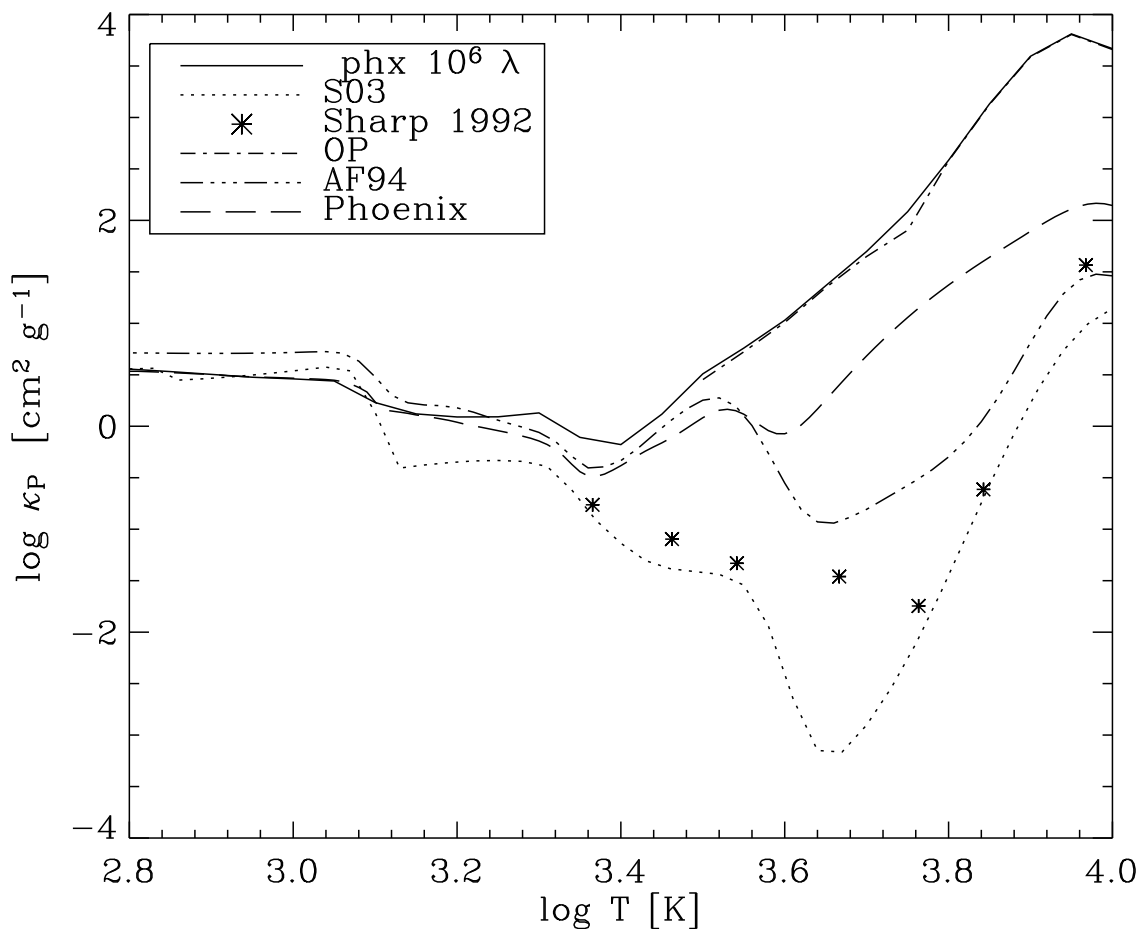


Fig. 12.— Total mean Planck opacity as a function of temperature for a single gas density of $10^{-10} \text{ g cm}^{-3}$. The solid line is a present calculation with over 1 million wavelength points in the wavelength integral. The long-dashed line is from the normal 24599 wavelength calculation discussed in the text. The dash-dot line is data from OP and the dash-dot-dot line is from AF94. The dotted line is data from Semenov et al. (2003) and the stars are from Sharp (1992).

presented here were performed at the Höchstleistungs Rechenzentrum Nord (HLRN), at the National Energy Research Supercomputer Center (NERSC), supported by the U.S. DOE, and at the San Diego Supercomputer Center (SDSC), supported by the NSF. We thank all these institutions for a generous allocation of computer time. FA acknowledges support from the PNPS and PNP CNRS programs, as well as to computing resources provided by CINES and IDRIS in France. We also acknowledge the support from the National Science Foundation under Grant No. EIA-0216178 and Grant No. EPS-0236913, matching support from the State of Kansas and the Wichita State University High Performance Computing Center.

REFERENCES

- Alexander, D. B. & Ferguson, J. W. 1994a, in IAU Colloq. 146: Molecules in the Stellar Environment, 149
- Alexander, D. R. 1975, *ApJS*, 29, 363
- Alexander, D. R. & Ferguson, J. W. 1994b, *ApJ*, 437, 879
- Alexander, D. R., Johnson, H. R., & Rypma, R. L. 1983, *ApJ*, 272, 773
- Allard, F. & Hauschildt, P. H. 1995, *ApJ*, 445, 433
- Allard, F., Hauschildt, P. H., Alexander, D. R., Tamanai, A., & Schweitzer, A. 2001, *ApJ*, 556, 357
- Allard, F., Hauschildt, P. H., Miller, S., & Tennyson, J. 1994, *ApJ*, 426, L39
- Allard, F., Hauschildt, P. H., & Schwenke, D. 2000, *ApJ*, 540, 1005
- Begemann, B., Dorschner, J., Henning, T., Mutschke, H., Guertler, J., Koempe, C., & Nass, R. 1997, *ApJ*, 476, 199
- Borysow, A. 2002, *A&A*, 390, 779
- Carbon, D. F. & Gingerich, O. 1969, in Proceedings of the 3rd Harvard-Smithsonian Conference on Stellar Atmospheres, Cambridge, Mass.: Massachusetts Institute of Technology (MIT), 1969, edited by Gingerich, Owen, p.377, 377
- Carlson, B. E., Prather, M. J., & Rossow, W. B. 1987, *ApJ*, 322, 559
- Chase, M. W., Davies, C. A., Downey, J. R., Frurip, D. J., McDonald, R. A., & Syverud, A. N. 1985, *J. Phys. Chem. Ref. Data*, 14, 1
- Chiosi, C., Bertelli, G., & Bressan, A. 1992, *ARA&A*, 30, 235
- Clayton, G. C., Wolff, M. J., Sofia, U. J., Gordon, K. D., & Misselt, K. A. 2003, *ApJ*, 588, 871
- Dowling, J. M. & Randall, C. M. 1977, in Infrared Emissivities of Micron-sized particles of C, MgO, Al₂O₃, and ZrO₂, at Elevated Temperatures, (El Segundo: The Aerospace Corporation)
- Egan, W. G. & Hilgeman, T. 1977, *Icarus*, 30, 413

- Eldridge, J. E. & Palik, E. D. 1985, in Handbook of Optical Constants, ed. E.D. Palik, (Orlando: Academic Press), 779
- Fabian, D., Henning, T., Jäger, C., Mutschke, H., Dorschner, J., & Wehrhan, O. 2001, A&A, 378, 228
- Gingerich, O., Noyes, R. W., Kalkofen, W., & Cuny, Y. 1971, Sol. Phys., 18, 347
- Gonzalez, J.-F., LeBlanc, F., Artru, M.-C., & Michaud, G. 1995, A&A, 297, 223
- Goorvitch, D. 1994, ApJS, 95, 535
- Goorvitch, D. & Chackerian, C. 1994a, ApJS, 91, 483
- . 1994b, ApJS, 92, 311
- Grevesse, N. & Noels, A. 1993, Origin and Evolution of the Elements
- Homeier, D., Allard, F., Hauschildt, P., Boudon, V., & Champion, J. 2004, ApJ, in prep.
- Huber, K. P. & Herzberg, G. 1979, Constants of Diatomic Molecules (New York: Van Nostrand Reinhold)
- Hudgins, D. M., Sandford, S. A., Allamandola, L. J., & Tielens, A. G. G. M. 1993, ApJS, 86, 713
- Husson, N., Bonnet, B., Scott, N. A., & Chedin, A. 1992, Journal of Quantitative Spectroscopy and Radiative Transfer, 48, 509
- Iglesias, C. A. & Rogers, F. J. 1991, ApJ, 371, 408
- . 1993, ApJ, 412, 752
- . 1996, ApJ, 464, 943
- Irwin, A. W. 1988, A&AS, 74, 145
- Jäger, C., Dorschner, J., Mutschke, H., Posch, T., & Henning, T. 2003a, A&A, 408, 193
- Jäger, C., Il'in, V. B., Henning, T., Mutschke, H., Fabian, D., Semenov, D., & Voshchinnikov, N. 2003b, Journal of Quantitative Spectroscopy and Radiative Transfer, 79, 765
- John, T. L. 1975, MNRAS, 172, 305
- . 1988, A&A, 193, 189

- . 1994, MNRAS, 269, 871
- Jørgensen, U. G. & Jensen, P. 1993, J. Molec. Spectrosc., 161, 219
- Jørgensen, U. G., Jensen, P., & Sorensen, G. O. 1994, in Poster Session Proceedings of IAU Colloquium 146: Molecular Opacities in the Stellar Environment. Edited by Peter Thejll and Uffe G. Jorgensen., p.51, 51–+
- Jørgensen, U. G., Jensen, P., Sørensen, G. O., & Aringer, B. 2001, A&A, 372, 249
- Jørgensen, U. G. & Larsson, M. 1990, A&A, 238, 424
- Koike, C., Kaito, C., Yamamoto, T., Shibai, H., Kimura, S., & Suto, H. 1995, Icarus, 114, 203
- Kurucz, R. 1993, Atomic data for opacity calculations. Kurucz CD-ROM No. 1. Cambridge, Mass.: Smithsonian Astrophysical Observatory, 1993., 1
- Littleton, J. E. & Davis, S. P. 1985, ApJ, 296, 152
- Lynch, D. W. & Hunter, W. R. 1991, in Handbook of Optical Constants II, ed. E.D. Palik, (Orlando: Academic Press), 396
- Martonchik, J. V., Orton, G. S., & Appleby, J. F. 1984, Appl. Opt., 23, 541
- Mathis, J. S., Rumpl, W., & Nordsieck, K. H. 1977, ApJ, 217, 425
- Mathisen, R. 1984, in Photo Cross Sections for Stellar Atmospheres Calculations – Compilation of References and Data, (Inst. of Theoret. Astrophys. Univ. of Oslo, Pub. Ser. No1.)
- Mutschke, H., Begemann, B., Dorschner, J., Guertler, J., Gustafson, B., Henning, T., & Stognienko, R. 1998, A&A, 333, 188
- Myerscough, V. P. & McDowell, M. R. C. 1966, MNRAS, 132, 457
- Neale, L., Miller, S., & Tennyson, J. 1996, ApJ, 464, 516
- Neale, L. & Tennyson, J. 1995, ApJ, 454, L169+
- Ordal, M. A., Bell, R. J., Alexander, R. W., Long, L. L., & Query, M. R. 1985, Appl. Opt., 24, 4493
- . 1987, Appl. Opt., 26, 744

- Ordal, M. A., Bell, R. J., Alexander, R. W., Newquist, L. A., & Querry, M. R. 1988, *Appl. Opt.*, 27, 1203
- Ossenkopf, V., Henning, T., & Mathis, J. S. 1992, *A&A*, 261, 567
- Partridge, H. & Schwenke, D. W. 1997, *J. Chem. Phys.*, 106, 4618
- Pegourie, B. 1988, *A&A*, 194, 335
- Philipp, H. R. 1985, in *Handbook of Optical Constants I*, ed. E.D. Palik, (Orlando: Academic Press), 719
- Phillips, J. G. & Davis, S. P. 1993, *ApJ*, 409, 860
- Pollack, J. B., Hollenbach, D., Beckwith, S., Simonelli, D. P., Roush, T., & Fong, W. 1994, *ApJ*, 421, 615
- Posch, T., Kerschbaum, F., Fabian, D., Mutschke, H., Dorschner, J., Tamanai, A., & Henning, T. 2003, *ApJS*, 149, 437
- Querry, M. R. 1985, in *Optical Constants* (Maryland: AChemical Research and Development Center)
- Reilman, R. F. & Manson, S. T. 1979, *ApJS*, 40, 815
- Ribarsky, M. W. 1985, in *Handbook of Optical Constants*, ed. E.D. Palik, (Orlando: Academic Press), 795
- Rogers, F. J. & Iglesias, C. A. 1992a, *ApJS*, 79, 507
- . 1992b, *ApJ*, 401, 361
- Rogers, F. J., Swenson, F. J., & Iglesias, C. A. 1996, *ApJ*, 456, 902
- Rosen, B. 1970, *Tables Internationales de Constantes Selectionnees*, 17, *Donnees Spectroscopiques Relatives aux Molecules Diatomiques* (New York: Pergamon Press)
- Rothman, L. S., Gamache, R. R., Tipping, R. H., Rinsland, C. P., Smith, M. A. H., Benner, D. C., Devi, V. M., Flaud, J.-M., Camy-Peyret, C., & Perrin, A. 1992, *Journal of Quantitative Spectroscopy and Radiative Transfer*, 48, 469
- Rouleau, F. & Martin, P. G. 1991, *ApJ*, 377, 526
- Saumon, D. & Chabrier, G. 1993, in *ASP Conf. Ser. 40: IAU Colloq. 137: Inside the Stars*, 307–+

- Schweitzer, A., Hauschildt, P. H., Allard, F., & Basri, G. 1996, MNRAS, 283, 821
- Seaton, M. J. & Badnell, N. R. 2004, MNRAS, 354, 457
- Seaton, M. J., Yan, Y., Mihalas, D., & Pradhan, A. K. 1994, MNRAS, 266, 805
- Semenov, D., Henning, T., Helling, C., Ilgner, M., & Sedlmayr, E. 2003, A&A, 410, 611
- Sharp, C. M. 1992, A&AS, 94, 1
- Sharp, C. M. & Huebner, W. F. 1990, ApJS, 72, 417
- Stothers, R. B. & Chin, C. 1991, ApJ, 381, L67
- Tropf, W. J. & Thomas, M. E. 1991, in Handbook of Optical Constants II, ed. E.D. Palik, (Orlando: Academic Press), 883
- Tsuji, T. 1966, PASJ, 18, 127
- . 1973, A&A, 23, 411
- Vardya, M. S. 1966, MNRAS, 134, 183
- Verner, D. A. & Yakovlev, D. G. 1995, A&AS, 109, 125
- Weck, P. F., Schweitzer, A., Stancil, P. C., Hauschildt, P. H., & Kirby, K. 2003, ApJ, 582, 1059
- Woitke, P. & Helling, C. 2004, A&A, 414, 335

Table 1. Improvements in Low Temperature Opacity Calculations

	A75 ^a	AJR ^b	AF94 ^c	Present work
Equation of State	super-saturation ratio	decoupled gas & dust	decoupled gas & dust	gas & dust in equilibrium
Molecular Opacity	straight mean	2×10^5 lines + straight mean water	3×10^7 lines	8×10^8 lines
Dust Opacity	1 species Rayleigh	3 species Mie	6 species CDE	31 species Mie
Number of Wavelengths	50	900	9000	24000+

^aAlexander (1975)

^bAlexander et al. (1983)

^cAlexander & Ferguson (1994a)

Table 2. Number of atomic lines for each ion

Element	I	II	III	IV	V
H	457				
He	1630	463			
C	8885	979	493	201	
N	13858	1725	402	499	233
O	2311	3954	1114	543	529
F	2363	2164	4919	889	273
Ne	4177	9119	860	838	220
Na	385	205	708	195	313
Mg	2668	580	846	1211	248
Al	869	3184	369	171	132
Si	8526	919	1539	326	131
P	2413	1213	163	214	221
S	834	1118	338	73	42
Cl	6982	1676	974	228	71
Ar	3838	10452	1726	160	80
K	702	67	633	111	153
Ca	12860	946	11740	82222	330004
Sc	191270	49811	1578	16985	130563
Ti	897313	264874	23742	5079	37610
V	1156793	925330	284003	61630	8427
Cr	434743	1304043	990951	366851	73222
Mn	327762	878996	1589314	1033926	450293
Fe	789192	1264969	1604934	1776984	1008385
Co	546132	1048188	2198940	1569347	2032402
Ni	149926	404556	1309729	1918070	1971819

Table 3. Thermodynamic and spectral line data for molecules

Molecule	Source of Thermo. data	Number of lines	Source of line data
H ₂ O	1	349,074,613	7
		101,455,142	8
		6,139,497	1
TiO	2	174,027,629	9
CH ₄	3	11,854,112	10
H ₃ ⁺	4	3,070,572	11
CN	2	2,245,378	12
SiO	2	1,429,165	13
ZrO	2	265,724	14
CO	2	134,421	15,16,17
MgH	2	162,621	18,19
VO	2	7,182	20
CrH	5	2,670	20
FeH	2	2,158	21
YO	2	975	22
C ₂	2	3,458,871	19
SiH	2	77,642	19
CH	2	71,569	19
NH	2	36,163	19
H ₂	6	28,486	19
OH	2	26,349	19

References.- (1) Allard et al. (1994); (2) Huber & Herzberg (1979); (3) Chase et al. (1985); (4) Neale & Tennyson (1995); (5) Tsuji (1973); (6) Saumon & Chabrier (1993); (7) Partridge & Schwenke (1997); (8) Jørgensen et al. (2001); (9) Allard et al. (2000); (10) Homeier et al. (2004); (11) Neale et al. (1996); (12) Jørgensen & Larsson (1990); (13) D. Carbon 1995, private communication; (14) Littleton & Davis (1985); (15) Goorvitch (1994); (16) Goorvitch & Chackerian (1994a); (17) Goorvitch & Chackerian (1994b); (18) Weck et al. (2003); (19) Kurucz (1993); (20) R. Freedman 1999, private communication; (21) Phillips & Davis (1993); (22) J. Littleton 1987, private communication.

Table 4. Thermodynamic and spectral line data for minor molecules

Molecule	Source of Thermo. data	Number of lines	Source of line data
O ₃	1	164,359	4
HNO ₃	1	117,476	4
CO ₂	2	59,883	4
NO ₂	1	55,406	4
SO ₂	2	26,225	4
N ₂ O	1	23,812	4
HOCl	1	13,300	4
OH	3	8,671	4
NO	3	7,319	4
CH ₃ Cl	2	6,687	4
ClO	1	5,966	4
NH ₃	2	5,787	4
H ₂ O ₂	1	5,444	4
H ₂ CO	1	2,701	4
PH ₃	2	2,886	4
C ₂ H ₂	2	1,258	4
OCS	2	737	4
HCN	2	772	4
HCl	3	371	4
N ₂	3	120	4
HF	3	107	4

References.- (1) Chase et al. (1985); (2) Irwin (1988); (3) Huber & Herzberg (1979) and Rosen (1970); (4) Rothman et al. (1992) and Husson et al. (1992).

Table 5. Thermodynamic and optical constant data for condensates

Condensate	Common name	Source of thermo. data	Source of optical constants	λ range	Analog
α -Al ₂ O ₃	Corundum	1	4	$0.21\mu \leq \lambda \leq 55.6\mu$	
γ -Al ₂ O ₃	Sapphire	1	5	$0.2\mu \leq \lambda \leq 400\mu$	
			6	$1\mu \leq \lambda \leq 7\mu$	
C	Carbon	2	7	$0.139\mu \leq \lambda \leq 300.42\mu$	
CaMgSi ₂ O ₆	Diopside	2			from Ca ₂ Al ₂ SiO ₇
Ca ₂ Al ₂ SiO ₇	Gehlenite	2	8	$6.69\mu \leq \lambda \leq 852\mu$	
Ca ₂ MgSi ₂ O ₇	Akermanite	2			from Ca ₂ Al ₂ SiO ₇
CaSiO ₃	Wollastonite	2			from MgSiO ₃
Ca ₂ SiO ₄	Larnite	2			from Mg ₂ SiO ₄
CaTiO ₃	Perovskite	2	9	$0.1\mu \leq \lambda \leq 1000\mu$	
Cu	Copper	1	10	$0.517\mu \leq \lambda \leq 55.6\mu$	
Fe	Iron	1	11	$0.2\mu \leq \lambda \leq 285.7\mu$	
FeS	Troilite	1	12	$0.1\mu \leq \lambda \leq 500\mu$	
Fe ₂ SiO ₄	Fayalite	2	13	$2.\mu \leq \lambda \leq 10000\mu$	
Fe ₂ O ₃	Hematite	1	14	$0.21\mu \leq \lambda \leq 55.6\mu$	
Fe ₃ O ₄	Magnetite	1	14	$0.21\mu \leq \lambda \leq 55.6\mu$	
H ₂ O (ice)	Water ice	3	15	$2.5\mu \leq \lambda \leq 200\mu$	
			16	$0.0992\mu \leq \lambda \leq 10000\mu$	
H ₂ O (water)	Water liquid	3	14	$1\mu \leq \lambda \leq 10^7\mu$	
MgAl ₂ O ₄	Spinel	1	17	$1\mu \leq \lambda \leq 300\mu$	
MgSiO ₃	Enstatite	1	18	$0.1\mu \leq \lambda \leq 624\mu$	
Mg ₂ SiO ₄	Forsterite	1	18	$0.1\mu \leq \lambda \leq 948\mu$	
MgTiO ₃	Geikeilite	1			from CaTiO ₃
MnS	Alabandite	1			from FeS
NH ₃	Ammonia ice	3	19	$1\mu \leq \lambda \leq 300\mu$	
NaCl	Salt	1	20	$1\mu \leq \lambda \leq 300\mu$	
Ni	Nickel	1	21	$0.667\mu \leq \lambda \leq 285.71\mu$	
Nb	Niobium	1	22	$1.24\text{\AA} \leq \lambda \leq 10.33\mu$	

Table 5—Continued

Condensate	Common name	Source of thermo. data	Source of optical constants	λ range	Analog
SiC	Moissanite	1	23	$0.1\mu \leq \lambda \leq 243.673\mu$	
α -SiO ₂	Silicon dioxide	1	24	$6.67\mu \leq \lambda \leq 487.4\mu$	
Ti	Titanium	1	11	$0.667\mu \leq \lambda \leq 200\mu$	
TiO ₂	Titanium dioxide	1	25	$1\mu \leq \lambda \leq 300\mu$	
ZrO ₂	Zirconium dioxide	1	26	$4.545\mu \leq \lambda \leq 95.238\mu$	

References.- (1) Chase et al. (1985); (2) Sharp & Huebner (1990); (3) Carlson et al. (1987); (4) Querry (1985); (5) Koike et al. (1995); (6) Begemann et al. (1997); (7) Rouleau & Martin (1991); (8) Mutschke et al. (1998); (9) Posch et al. (2003); (10) Ordal et al. (1985); (11) Ordal et al. (1988); (12) Egan & Hilgeman (1977); (13) Fabian et al. (2001); (14) Querry (1985); (15) Hudgins et al. (1993); (16) Pollack et al. (1994); (17) Tropf & Thomas (1991); (18) Jäger et al. (2003a); (19) Martonchik et al. (1984); (20) Eldridge & Palik (1985); (21) Ordal et al. (1987); (22) Lynch & Hunter (1991); (23) Pegourie (1988); (24) Philipp (1985); (25) Ribarsky (1985); (26) Dowling & Randall (1977).